Building Hierarchical Martensite

*Stefan Schwabe, Robert Niemann, Anja Backen, Daniel Wolf, Christine Damm, Tina Walter, Hanuš Seiner, Oleg Heczko, Kornelius Nielsch, and Sebastian Fähler**

Martensitic materials show a complex, hierarchical microstructure containing structural domains separated by various types of twin boundaries. Several concepts exist to describe this microstructure on each length scale, however, there is no comprehensive approach bridging the whole range from the nano- up to the macroscopic scale. Here, it is described for a Ni-Mn-based Heusler alloy how this hierarchical microstructure is built from scratch with just one key parameter: the tetragonal distortion of the basic building block at the atomic level. Based on this initial block, five successive levels of nested building blocks are introduced. At each level, a larger building block is formed by twinning the preceding one to minimize the relevant energy contributions locally. This naturally explains the coexistence of different types of twin boundaries. The scale-bridging approach of nested building blocks is compared with experiments in real and reciprocal space. The approach of nested building blocks is versatile as it can be applied to the broad class of functional materials exhibiting diffusionless transformations.

1. Introduction

Twin boundaries (TBs) connecting different orientations of the unit cell are the characteristic feature of a martensitic microstructure. This microstructure forms after a diffusionless structural transformation from a high temperature austenite to a low temperature martensite phase. Commonly, TBs are observed at all length scales, from the nano- up to the macroscale. Such a hierarchical, twins-within-twins microstructure is found in many different materials including high strength martensitic steel[1] or NiTi as a prototype shape memory alloy.[2] A similar microstructure can also be observed in several ferroelectric[3] and multiferroic[4] materials. Ni-Mn-based Heusler alloys[5] are of particular interest as they exhibit several emerging functional properties. They can be used to convert waste heat into electricity by thermomagnetic energy harvesting[6] or provide a more energy efficient cooling using magnetocaloric,[7] elastocaloric,[8] or multicaloric effects.[9] Furthermore, they are utilized for high stroke actuation by either magnetically induced reorientation[10] or a magnetically induced phase transformation.[11]

Despite the broad range of hierarchical materials, no comprehensive approach exists that can describe the crystallographic features of the martensitic microstructure across all length scales. Most descriptions and experiments consider just one length scale, e.g., the adaptive concept[12] describes merely one part of the nanoscale. Similar limitations also hold for other methods like density functional theory[13] or molecular dynamics.[14] On the other hand, the non-linear continuum mechanics framework derived by Ball and James[15] and presented in detail in the textbook of Bhattacharya,[16] is based just on total static energy minimization without incorporating the sequence how the microstructure is built. Hence, this scale invariant continuum-based theory cannot directly predict the observed deep level of hierarchy. Although for particular length scales a good agreement between theory and experiment exists,[17] there is only one approach explaining all length scales in a hierarchical microstructure.[18] It was suggested that a stepwise compensation of each strain component occurs at every level. However, recent in situ experiments indicate that the concept of global energy equilibrium is not appropriate.[5b] This leads to the question: Is a scale-bridging description of the experimentally observed hierarchical martensitic microstructure possible, which considers the constraints of the transformation path? It should be simple, originating from some fundamental properties of the lattice.

To resolve this question, we choose the well-studied Heusler alloy Ni–Mn–Ga as our model system and investigate it comprehensively by looking at all length scales within the real space (Section 2: The quest) as well as reciprocal space (Section 2.6: Bonus level). This enables us to answer two additional questions: Are there "building blocks," which are connected by the

S. Schwabe, Dr. R. Niemann, Dr. A. Backen, Dr. D. Wolf, C. Damm,
T. Walter, Prof. K. Nielsch, Dr. S. Fähler
Leibniz IFW Dresden
Helmholtzstraße 20, Dresden 01069, Germany
E-mail: s.faehler@ifw-dresden.de
S. Schwabe, Prof. K. Nielsch
TU Dresden
Institute of Materials Science
Dresden 01062, Germany
Dr. H. Seiner
Czech Academy of Sciences
Institute of Thermomechanics
Prague 18200, Czech Republic
Dr. O. Heczko
Czech Academy of Sciences
Institute of Physics
Prague 18221, Czech Republic

**ADVANCED
SCIENCE NEWS**

www.advancedsciencenews.com

**ADVANCED
FUNCTIONAL
MATERIALS**

www.afm-journal.de

different types of TBs observed at each length scale; and does the energy minimization happen on the local scale of these TBs?

Starting with the basic tetragonal unit cell that results from the cubic to tetragonal structural transition, our approach considers five levels built upon one another. It allows a seamless connection of nano-twinning proposed in the adaptive concept[12] with continuum mechanics[15–16] by using the recent concept of ordering nanotwins.[19] In **Figure 1**, an overview of our model is sketched, which acts as an outline of this paper. On each level, a new building block is introduced, which is used to construct the next higher level, similar to a computer game. Every single level is explained in detail after introducing the experimental findings. Though some levels are already well understood, their connections are mostly missing. We can demonstrate a seamless connection between all levels and that the distortion of the tetragonal building block on level 0 is the key parameter sufficient for defining most of the martensitic microstructure.

2. The Quest: Identifying Twin Boundaries and Building Blocks on all Length Scales

Before summarizing the experimental findings, we introduce some general terms. A hierarchical microstructure has several common features at all length scales. For each level shown in Figure 1, we will identify the smallest building block sufficient for the construction of the martensitic microstructure at that level. Regions with equally oriented building blocks are called variants. A twin boundary (TB) connects two variants of different orientation. The TB must satisfy the so-called condition of kinematic compatibility,[16] which ensures that it can exist without long range stress fields. According to the symmetry operation connecting both variants, three different symmetries of TBs are established: type I TBs, type II TBs and compound TBs, as described in more detail in reference.[16] Furthermore, we will use the term laminate for regions of parallel TBs. As these terms are used at all levels, the associated length scale will always be included.

To illustrate the hierarchical microstructure, we use an epitaxial Ni–Mn–Ga film grown on MgO (001) as a model system. Similar to single crystals, this has the advantage that its martensitic microstructure is not disturbed by grain boundaries within the austenite. In addition, the MgO substrate provides a fixed reference frame. As a starting point, we sort all the TBs into the different levels and identify the building blocks. For this purpose, a zoom-in into the hierarchical microstructure is shown in **Figure 2**. According to the common approach, here we start at the macroscopic scale working our way toward the nanoscale. The scanning electron microscopy (SEM) image in Figure 2a (see also Figure S1 in the Supporting Information for a larger area) shows a macroscopic top view. It displays two notably different microstructures of almost parallel lines. We call them type X (lines under 45° to the picture borders) and type Y (lines parallel to the picture border).[20] They are also known as high contrast zone and low contrast zone.[21] At the largest length scale, macroscopic TBs[22] (brown) are apparent (cf. also Figure 1, level 5), which are sometimes called colony boundaries.[5a] They occur where two differently aligned type X and/or type Y zones meet.
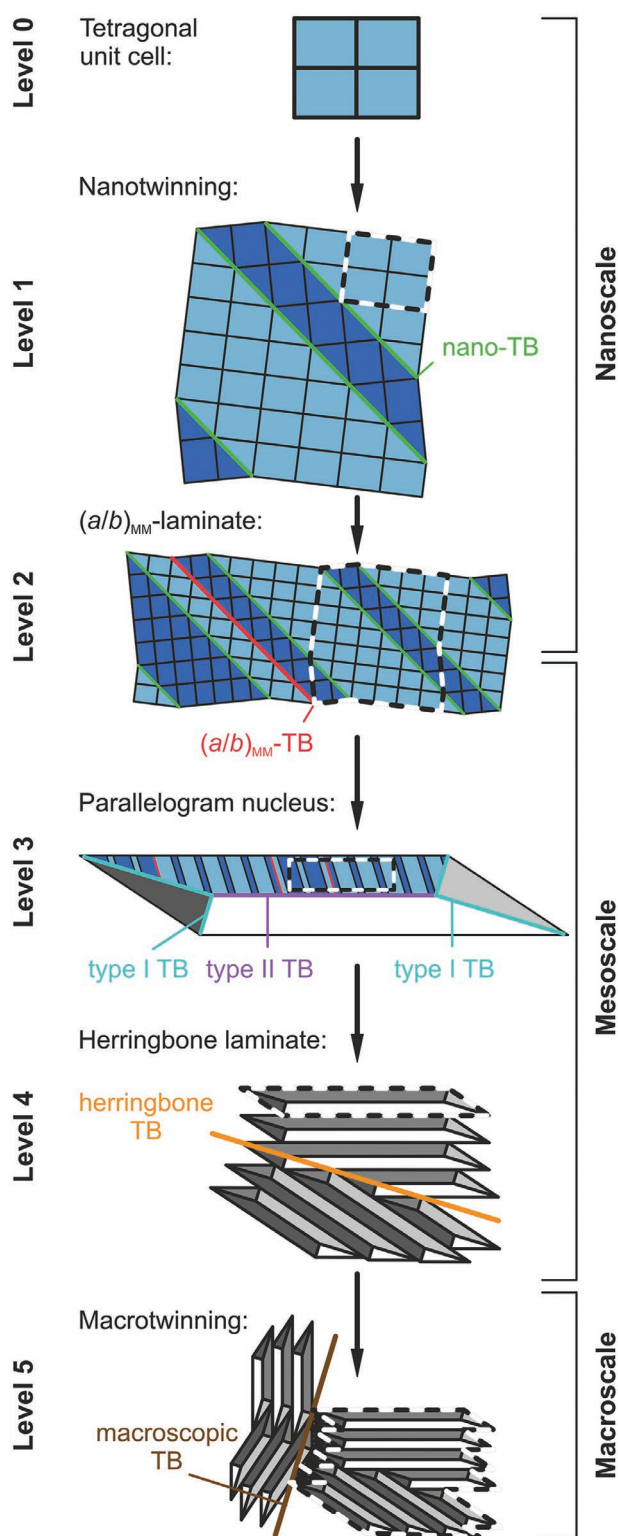

Figure 1. Overview of nested building blocks and twin boundaries (TB) from the nano- to the macroscale. The microstructure development is classified into levels, starting with the basic tetragonal cell at "level 0." In each subsequent level, a new building block is introduced. It is constructed by combining the building blocks from the previous level by twinning (highlighted in different colors). The levels can be assigned to their typical length scales from the nano- to the macroscale.
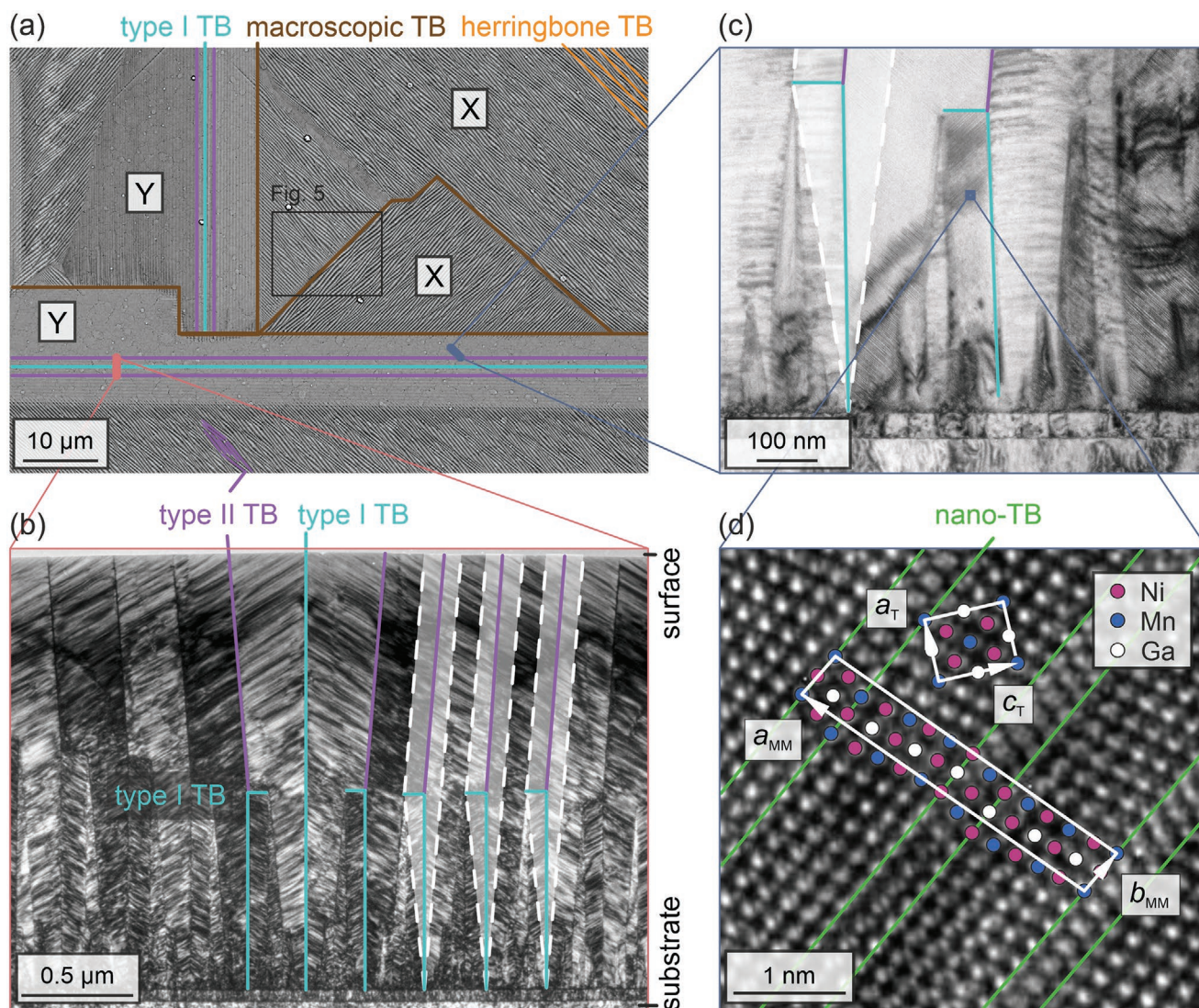
Figure 2. Zoom into a hierarchical microstructure with five different types of twin boundaries (TB), which are selectively highlighted. a) Macroscopic top view showing areas of differently aligned laminates (type X and Y) observed by SEM (backscattered electron contrast). These laminates are connected by macroscopic TBs (brown) and incorporate mesoscopic TBs, mainly type II (purple) and a few type I TBs (cyan). To differentiate between these two, it is helpful to look at the cross-sections. Type II TBs form a characteristic herringbone laminate discussed in more detail on level 4 observing the area framed in black. The figure edges are parallel to $[110]_A$ and $[\bar{1}10]_A$, respectively. b) The mesoscopic scale revealed by bright-field (BF)-TEM of a few tens' nanometer thin cross-section sample (position marked red in (a)). The important TBs at this length scale are type I and type II TBs. Martensitic nuclei are sketched in white in an intermediate growth stage, when they just reach the substrate. The dashed white lines denote the interface to the austenite at this moment (not visible anymore in the fully transformed sample). c) BFTEM image of a second cross-section cut rotated by 45° with regard to (b). This enables us to see the modulations at the nanoscale. d) HR-TEM image revealing the periodically arranged nano-TBs (green) zooming into the area marked with a blue square in (c). A modulated, monoclinic unit cell (with in-plane axes a_{MM} and b_{MM}) is marked as well as the tetragonal building block (axes a_T and c_T). The atom mapping is chosen arbitrary as all columns of atoms have almost the same contrast. This figure without the overlays is available in the Figure S2, Supporting Information.

Most of the visible lines within type X and type Y have been identified as mesoscopic type II TBs (purple) together with some type I TBs (cyan), as described previously.[23] In type X areas, a herringbone laminate is visible (level 4), incorporating herringbone TBs (orange). The characteristics of the mesoscopic TBs become clearer when looking at the transmission electron microscopy (TEM) image of the cross-section through type Y martensite (Figure 2b) marked by a red line in Figure 2a. Two types of TBs can be distinguished[5b] differing by their angle toward the substrate: type I TBs (cyan) and type II TBs (purple). Martensitic nuclei are sketched in white in an intermediate growth stage, when they just arrive at the substrate, described in more detail in Section 2.3 (level 3).

A TEM image of a second cross-section (blue), cut 45° rotated in-plane compared to Figure 2b, is shown in Figure 2c. It allows identifying the features at the atomic scale as shown in a further high resolution (HR)-TEM zoom-in (Figure 2d). The investigated region is marked by a blue square in Figure 2c. As

**ADVANCED
SCIENCE NEWS**

www.advancedsciencenews.com

**ADVANCED
FUNCTIONAL
MATERIALS**

www.afm-journal.de

reported in detail by various other groups,[24] at this smallest length scale modulations become visible, which can be identified as nano-TBs[12] (green). Nano-TBs connect differently aligned orientations of a tetragonal building block of a non-modulated martensite with the axes a_T and c_T (level 1).[25] The ratio of both axes (c_T/a_T-ratio) is the key parameter used for our model, as it characterizes the simplest and smallest building block. For our particular sample, five atomic planes shift in one direction followed by two planes shifting in the opposite direction. Preserving the chemical order, this is a 14M modulated martensite (MM) exhibiting a $(5\bar{2})_2$ modulation in Zhdanov notation (Figure 2d).

To sum up, these micrographs at different zoom levels demonstrate that all different types of TBs coexist in one sample and are nested into each other.

2.1. Level 1: Formation of a Modulated Unit Cell by Nanotwinning

We start our description at the atomic scale with the fundamental transition between austenite (lattice parameter a_A) and tetragonal martensite (lattice parameters a_T and c_T) as sketched in **Figure 3**a. This transition occurs due to the lower free energy of the tetragonal phase below the transition temperature. The tetragonal distortion c_T/a_T can be estimated from DFT calculations and is typically around 1.25 for Ni_2MnGa.[26] However, as these calculations commonly consider the situation at zero Kelvin, they usually overestimate the value. In addition, the c_T/a_T-ratio can be influenced by chemical composition and order, and thus it differs for different samples.

In the following, we use this ratio as our key parameter to construct a modulated unit cell. Generally, the tetragonal distortion can occur in each of the three spatial directions. However, on this level it is sufficient to consider only the two tetragonal cells sketched in dark and light blue color in Figure 3a. Furthermore, it is convenient to subdivide the austenite and the tetragonal martensite cells into smaller "building blocks."[25] These smaller blocks have just half the lattice parameters of chemically ordered Heusler alloys.

The transition is of first order; therefore, austenite and martensite must coexist. They form a compatible phase boundary between them, called "habit plane," which ideally has a minimum of excess interface energy. As martensitic transitions are diffusionless, the number of building blocks on both sides of this habit plane must be equal, which leaves the orientation of the building blocks as the only way to minimize energy. If a single orientation of tetragonal building blocks were connected to the same number of austenite ones, there would be a huge elastic deformation due to the large lattice misfit. To reduce this misfit and thus the elastic energy, it is favorable to combine a particular ratio of tetragonal blocks differing in the direction of their long axis (light and dark blue in Figure 3c). This is done by introducing nano-TBs (Figure 3b), requiring only low excess energy. The resulting twinned arrangement forms a compatible habit plane (sketched in Figure 3c). On both sides of the habit plane, the number of building blocks as well as their total length is equal.

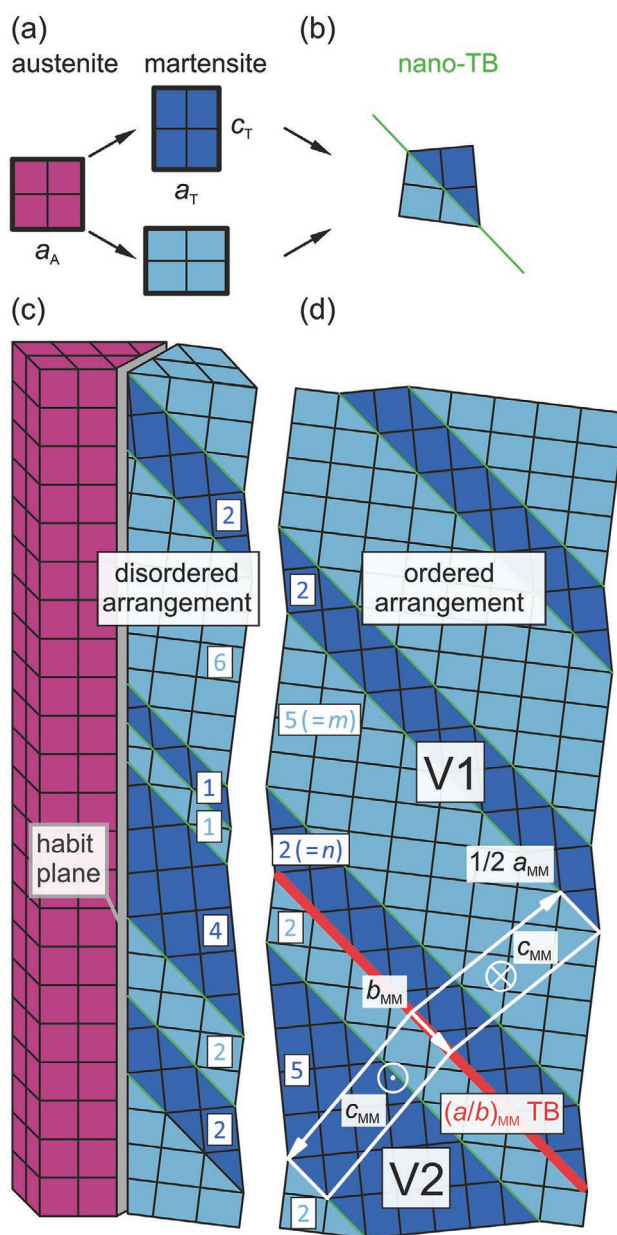The distance between TBs in this nano-laminate can be determined by applying continuum theory:[12] the sum of excess

Figure 3. Construction of the building blocks for level 1 (modulated unit cell) and level 2 (($a/b)_{MM}$-laminate) using the basic tetragonal cell. a) 2D projection of the fundamental phase transition from the cubic austenite (magenta) to the tetragonal martensite (blue) when cooling below the martensitic transition temperature. The tetragonal building blocks can occur in two orientations, depicted in light and dark blue. b) Twin boundaries (TB) between both orientations of the tetragonal unit cell are called nano-TBs (green line). c) Disordered arrangement of nano-TBs forming a habit plane to the austenite. To illustrate that at the nano scale some disturbance of the lattice occurs, the habit plane is drawn as a gray region. d) Sketch of the consequence of the interaction energy between nano-TBs leading to a transformation to a periodic (ordered) arrangement (($5\bar{2})_2$-stacking). Because of this ordering process, a modulated structure as well as ($a/b)_{MM}$-TBs form (red line). The regions that are separated by ($a/b)_{MM}$-TBs are again variants according to our definition. The ($a/b)_{MM}$-TB is a mirror plane between variant 1 (V1) and V2. They have a monoclinic, modulated unit cell (surrounded by white lines). In a_{MM}-direction, only half of this cell is sketched. To account for the chemical order in Heusler alloys, the unit cell would be twice as long.

**ADVANCED
SCIENCE NEWS**
www.advancedsciencenews.com

**ADVANCED
FUNCTIONAL
MATERIALS**
www.afm-journal.de

energy of all TBs together with the elastic energy of a habit plane must be minimized. According to the adaptive concept,[12] a low specific TB energy and a large shear modulus can favor a reduction of the distance between TBs down to the finite size of the building blocks. This is applicable for the particular Ni_2MnGa system,[27] which explains the occurrence of nano-TBs as the first level of TBs, having a very narrow spacing.

In the textbook case,[28] an irregular arrangement of nano-TBs (cf. Figure 3c) can minimize the elastic energy at the habit plane as they just have an excess energy. Recently however, an additional interaction energy was introduced[19] explaining the quite periodic modulations observed in experiments (cf. Figure 3d). In our sample, a $(5\bar{2})_2$-stacking is present. At level 1, we consider only the upper part of Figure 3d (above the red line), which we will call "variant 1" (V1).

We assign n to be the number of building blocks with their long axis approximately parallel to the habit plane (dark blue). The number of light blue blocks is specified by m. As in our martensitic Heusler alloy the c_T/a_T-ratio is > 1, one needs more light blue than dark blue building blocks for length conservation, meaning $m > n$. According to the concept of ordering nanotwins,[19] $n = 2$ is favored due to a minimum of interaction energy between the nano-TBs. To determine m, we consider that at the habit plane the number of unit cells and their length for austenite and martensite must be equal

$$(n+m) \cdot a_A = n \cdot c_T + m \cdot a_T \tag{1}$$

In this equation, we neglect the small angle of only a few degrees between the axes of the tetragonal cell and the austenite unit cell. To solve this equation for m, we measured $a_A = 5.828$ Å by X-ray diffraction (see Figure S3, Supporting Information). Furthermore, the change of volume at the martensitic transformation can be as low as 0.06%,[29] making volume conservation a good approximation: $a_A^3 = c_T \cdot a_T^2$. This introduces a dependence of c_T and a_T and allows us to reduce the number of variables further, leading to the c_T/a_T-ratio as our key parameter.

The number of unit cells must be an integer. In a descriptive picture, this means that a small gap occurs between $(n + m)$ austenitic building blocks on one side of the habit plane and the sequence of n dark blue and m light blue tetragonal building blocks on the other side. For $c_T/a_T = 1.205$ of our particular sample (cf. Section 2.6: Bonus level), the resulting m has to be rounded up to the next integer. This gives $m = 5$, and therefore the $(5\bar{2})_2$-stacking of 14M is expected and observed.

This ordered arrangement of nano-TBs allows introducing a larger unit cell with a monoclinic symmetry (sketched in white in Figure 3d). Only half of the cell is shown in the a_{MM} direction due to the limited space. All four lattice parameters of this modulated unit cell can be calculated directly from the c_T/a_T-ratio by elementary geometry (see Supporting Information) using the volume conservation from above. For the particular sample, we obtain: $a_{MM} = 29.60$ Å, $b_{MM} = 4.29$ Å, $c_{MM} = 5.48$ Å and $\gamma_{MM} = 85.4°$. As interaction energy can stabilize a modulated unit cell,[19] we consider it as a stable building block for all following levels.

As in experiments sometimes commensurate and incommensurate modulated phases are observed,[30] it is interesting to reconsider the similarity of the constraint at a habit plane with a classical model system. The 1D Frank and Van der Merwe (FVdM) model[31] describes an array of atoms connected with harmonic springs interacting with a periodic potential. Following the review of Bak,[32] different arrangements of the atoms can occur when the periods of atoms and potentials differ. In case of a strong interaction and low temperatures, commensurate arrangements form, otherwise incommensurate arrangements are possible. Indeed, for the particular Ni–Mn–Ga system both arrangements are experimentally observed[17c,30] and subtle changes in composition and temperature seem to decide, which one is preferred. Furthermore, the FVdM model allows also for chaotic, fluid like arrangements, which have a striking similarity to the premartensitic phase, first reported by Zheludev et al.[33] as precursor above the martensitic transformation temperature. The constraints at a habit plane are more complicated than the FVdM model since twinning results in a double well potential, as both a_T and c_T can be aligned in parallel to the habit plane. Nevertheless, we propose that the mostly observed modulations in Ni–Mn–Ga ($(5\bar{2})_2$ and $(3\bar{2})_2$) are part of a "devil staircase,"[32] which is a common phase diagram for a FVdM model.

To sum up this level, the constraint to form a phase boundary makes the introduction of TBs at the nanoscale necessary. As they require only a low excess energy, they can be introduced at a high density.

2.2. Level 2: Formation of an $(a/b)_{MM}$-Laminate

On this level, we have to deal with the remaining small length difference between the unit cell of modulated martensite and austenite, described before. With increasing number of unit cells, this difference accumulates and results in an increasing elastic energy. To reduce this energy, the same mechanism as described for the tetragonal blocks is used: the introduction of TBs. This results in an alternating direction of the modulated cells connected by $(a/b)_{MM}$-TBs (marked red in Figure 3d). This type of TB had recently been described experimentally[34] as well as theoretically by the concept of ordering nanotwins.[19] An $(a/b)_{MM}$-TB connects two variants V1 and V2 with interchanged ratios of the light and dark blue orientations, respectively. An appropriate length ratio λ of both variants within an $(a/b)_{MM}$-laminate allows to adapt exactly to the habit plane (for the particular sample, $\lambda = 0.875$, calculation described on level 3). As each $(a/b)_{MM}$-TB coincides with a nano-TB, they are expected to have only a small excess energy in the same order as the interaction energy. This makes $(a/b)_{MM}$-TBs, out of all theoretically possible TBs,[23] the most favorable to form an exact habit plane.[19] In agreement with this, they are also observed for 10M martensite with a very narrow spacing,[35] showing even some refinement.[36]

To sum up level 2, the formation of $(a/b)_{MM}$-TBs is required to further reduce the phase boundary energy. In contrast to level 1, which considers integer numbers of building blocks, level 2 allows using continuum theory, as described in detail within level 3.

ADVANCED
SCIENCE NEWS
www.advancedsciencenews.com

ADVANCED
FUNCTIONAL
MATERIALS
www.afm-journal.de

2.3. Level 3: Nucleation of Martensite

The aim for this level is to use the $(a/b)_{MM}$-laminate as a building block to construct martensitic nuclei. First order transformations proceed through nucleation, which requires the encapsulation of a volume of martensite within the austenite using boundaries that have a minimum of interface energy. This aspect cannot be solved completely on level 2, as a single $(a/b)_{MM}$-laminate only forms a single habit plane. Thus, in this level we need to identify combinations of habit plane variants suitable for the nucleation of martensite, which are both, compatible with the austenite and to each other.

For the precise construction of a nucleus, we apply nonlinear continuum mechanics.[15–16] This continuum theory uses lattice parameters and symmetry of both phases as input parameters and predicts the orientations of all variants forming the $(a/b)_{MM}$-laminates as well as the habit planes. Thus, this theory suits our approach of nested building blocks, as the lattice parameters of the modulated unit cell were already obtained at level 1 using the c_T/a_T-ratio. Furthermore, due to the energetic arguments of level 2, favoring $(a/b)_{MM}$-TBs at the habit plane, it is sufficient to consider only these laminates, which are summarized in Table S2 (Supporting Information).

As a result, we obtain habit planes, which are close to $\{1\,0\,1\}_A$, but have a slight deviation. For better readability, we often refer to them using just the approximate austenite planes. Nevertheless, the slight deviation from $\{1\,0\,1\}_A$ is important, as it allows to encapsulate a volume of martensite by combining several habit planes.[5b] The simplest solution is the combination of eight habit planes in the shape of a diamond as sketched in **Figure 4**a, which was directly observed by in situ experiments.[5b] Each of the eight habit planes connects austenite with a particular orientation of an $(a/b)_{MM}$-laminate. To illustrate the nesting of building blocks, the inset depicts the orientation of nano- and $(a/b)_{MM}$-TBs inside one laminate. All laminates within one diamond can be transformed into each other by mirroring them along the planes going through the middle of the diamond. These "midribs" are thus compatible TBs. As they occur at the mesoscale, we call them mesoscopic TBs. Their interface energies must be provided to enable nucleation. Using the common nomenclature,[23] the midribs of a diamond can be identified as type I TBs (two are marked cyan and the third one coincides with the austenite $(1\,\overline{1}\,0)_A$ plane in Figure 4a).[5b] For a better comparison with the observed microstructure, the diamond is viewed along its longest axis in Figure 4b. In this viewing direction, the vertical type I TB corresponds to the one that lies within the austenite $(1\,\overline{1}\,0)_A$ plane. More information regarding the martensitic variants used to construct the diamond nucleus is given in Table S3 (Supporting Information).

Such a nucleus has the characteristic opening angles α and β. It can transform to a more complex, parallelogram shaped nucleus geometry by selectively extending some of the eight habit planes,[5b] as illustrated in Figure 4c. This transformation was confirmed recently also for bulk samples.[37] Within such a nucleus, an additional type II TB (purple) forms, which is known for its extraordinarily low twinning stress.[38] The type II TB is slightly inclined by the angle $\alpha/2$ from the $(1\,\overline{1}\,0)_A$ plane. In situ experiments revealed the transformation from a diamond into a parallelogram as thus additional volume can be transformed once a diamond reaches incompatible boundaries during growth.[5b]

Both nuclei as a whole are only fully compatible when assuming volume conservation at the transition. In case of a volume change, long-range stress fields occur, which will be treated elsewhere.[39] Diamonds and parallelograms are the only geometries with internally compatible interfaces and a minimal number of eight habit planes. Accordingly, for the formation of these geometries only a low energy barrier has to be overcome, which paves the way for nucleation.

Following the concept of nested building blocks, the geometry of both types of nuclei is fully determined by the c_T/a_T-ratio
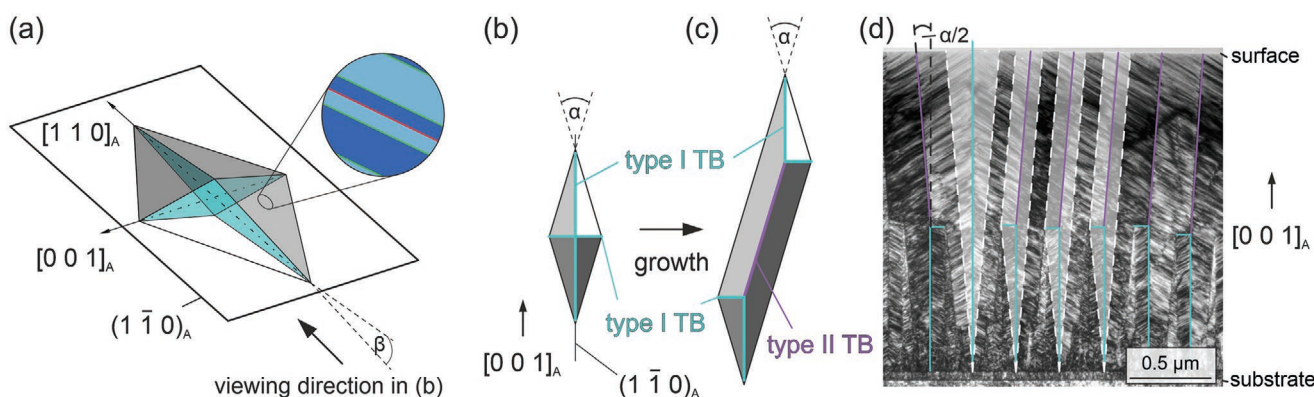

Figure 4. On level 3, $(a/b)_{MM}$-laminates are used as building blocks for diamond and parallelogram nuclei. a) Sketch of a diamond shaped nucleus, consisting of eight differently aligned $(a/b)_{MM}$-laminates. As illustrated by the zoom-in, each of them includes nano-TBs (green lines) and $(a/b)_{MM}$-TBs (red line). The midribs of this diamond consist of three type I TBs (two are marked cyan and the third one correlates with the austenite $(1\overline{1}0)_A$ plane). b) Frontal view of the nucleus as indicated in (a). The vertical type I TB is the one that lies in the austenite $(1\overline{1}0)_A$ plane. c) The growth of a diamond into a parallelogram nucleus introduces an additional type II TB (purple). d) Overlay of a section of the TEM cut (from Figure 2b) with parallelogram nuclei. To reduce the total interface energy, only the bottom part of the parallelogram occurs in a thin film. As this sample has fully transformed, the dashed white lines mark the position of the habit plane between austenite and martensite in an intermediate state during the transition, when the nuclei just reach the substrate. By merging with neighboring nuclei during growth, identity boundaries form, which are therefore not visible. In all sketches, the angles α and β are increased in order to improve visibility of all features.

ADVANCED
SCIENCE NEWS
www.advancedsciencenews.com

ADVANCED
FUNCTIONAL
MATERIALS
www.afm-journal.de

(see Supporting Information code). For the particular sample with a c_T/a_T-ratio of 1.205, we obtain $\lambda = 0.875$, $\alpha = 10.5°$, and $\beta = 3.1°$. This high value of λ means that the habit planes are dominated by the variant V1 (cf. Figure 3d) and only a small fraction of V2 occurs. The characteristic geometries and angles can also be found in the cross-section TEM image for the type Y structure (Figure 4d), suggesting that the shape of these building blocks is conserved during growth. The average angle between the type I and type II TB ($\alpha/2$) was measured to be around 4.5° using the TBs shown in Figure 4d. The dashed white lines visualize the habit plane in an intermediate state during growth, when the nuclei just reach the substrate. A nucleus can save some of its total mesoscopic TB energy by moving partly out of the film. This agrees with the shown cross-section, where one tip of the nucleus is not visible. All nuclei consist of the same set of eight variants and diagonally opposing variants within one nucleus are identical. Thus, when they meet often no TB is visible after the coalescence of two neighboring nuclei; the previous habit planes become an "identity boundary." The TBs of the nuclei forming the type X structure can be identified by looking at the sample surface, which is shown in Figure S4 (Supporting Information).

To sum up level 3, mesoscopic TBs originate from the need to nucleate the martensite phase. Nucleation as a local process prefers interfaces with minimum energy, which explains why only geometries with compatible habit planes and TBs are observed.

2.4. Level 4: Growth of Martensite toward a Herringbone Laminate

The growth of martensite is driven by the lower free volume energy of the martensite phase compared to austenite below the transformation temperature. Accordingly, nuclei grow as large as possible, but this growth is limited by incompatible boundaries, which would require an additional interface energy. Examples of incompatible boundaries are grain boundaries, the interface to the substrate, or regions that had already transformed to the martensite before. When a diamond meets an incompatible boundary during growth, it may transform to a parallelogram for further growth,[5b] but when this parallelogram meets the next incompatible boundary afterward, it cannot grow further. This determines the length scale, which is not predicted by continuum mechanics. Thus, many diamonds and parallelograms are required to transform polycrystalline materials or films on rigid substrates compared to a single crystal.

A way to transform most of the volume while avoiding incompatible boundaries is sketched in 2D within the blue shaded area of **Figure 5**a. Diamond and parallelogram nuclei are used as building blocks to assemble a self-accommodated herringbone laminate. A diamond nucleus has two equivalent possibilities to transform into parallelograms. Accordingly, herringbone TBs (orange) are introduced, which connect both parallelogram orientations. These TBs therefore originate from the spontaneous symmetry reduction when transforming diamonds to parallelograms. As these nuclei originate from the same $\{1\,1\,0\}_A$ plane, they fit together because they are surrounded by the same set of habit planes. The microstructure of a herringbone laminate is characterized by the angle α (cf. Figure 4c) of its building blocks. In order to enable a comparison with experiment, a Fourier transformation of an area containing only type X martensite was done (Figure S5, Supporting Information) and gives $\alpha = 8.8°$ ($\alpha/2 = 4.4°$). This nearly matches the $\alpha/2 = 4.5°$ measured for the type Y martensite (Figure 4d) and is in reasonable agreement with the value of $\alpha/2 = 5.25°$ obtained from continuum mechanics for $c_T/a_T = 1.205$.

In thin films, the growth of the nuclei is limited by the substrate. Due to the constant film thickness, a very homogenous spacing of mesoscopic TBs is observed in our single-crystal-like films. The spacing of the herringbone TBs is likely governed by a minimization of elastic energy. For this, both orientations of the parallelogram nuclei (cf. Figure 5a) are needed as the growth direction of each one slightly differs from the herringbone TB. Therefore, the occurrence of only one type of parallelogram nucleus would raise the elastic energy, when the size of the transformed area increases.

In case of a polycrystalline sample, typically the size of the mesoscopic building blocks becomes smaller when approaching an incompatible grain boundary.[40] Furthermore, the shape of the nuclei appears to be different in each grain. This is because each grain has a distinct orientation and therefore a different cross section of the 3D nuclei is visible.

As the tips of the nuclei forming the herringbone laminate have their characteristic angles α and β, a gap remains when they reach incompatible boundaries, as can be seen for the type Y cross-section in Figure 4d and for the type X martensite in Figure 5c. This gap can be filled with another nucleus, because the new nucleus has the complementary angle. While in bulk samples these new nuclei can have a similar size, this is not the case for thin films, where the remaining space toward the substrate is smaller. Accordingly, the nuclei toward the substrate become smaller and smaller. During this refinement of the martensitic microstructure, the ratio between volume and TB area of the nuclei decreases, which is similar to classical branching toward the austenite-martensite interface.[41] As mesoscopic TBs require an additional excess energy,[42] we expect that a higher undercooling below the transformation temperature is necessary to fill the remaining, small regions. This refinement is also observed at incompatible macroscopic TBs (Figure 5b).

To sum up level 4, the spontaneous reduction of symmetry when transforming a diamond to a parallelogram enables and requires a herringbone TB.

2.5. Level 5: Macrotwinning

Here, the herringbone laminate is used as a building block. We follow the same approach as already used at level 1, where the laminate of nano-TBs forms the modulated unit cell. At the nanoscale, we could even calculate symmetry and lattice parameters of this building block. For the macroscale, we give a more general description. The habit planes forming the martensitic nuclei of the herringbone laminate in Figure 5a (blue part) are all close to one particular $\{1\,0\,1\}_A$ plane sketched in blue in

**ADVANCED
SCIENCE NEWS**

www.advancedsciencenews.com

**ADVANCED
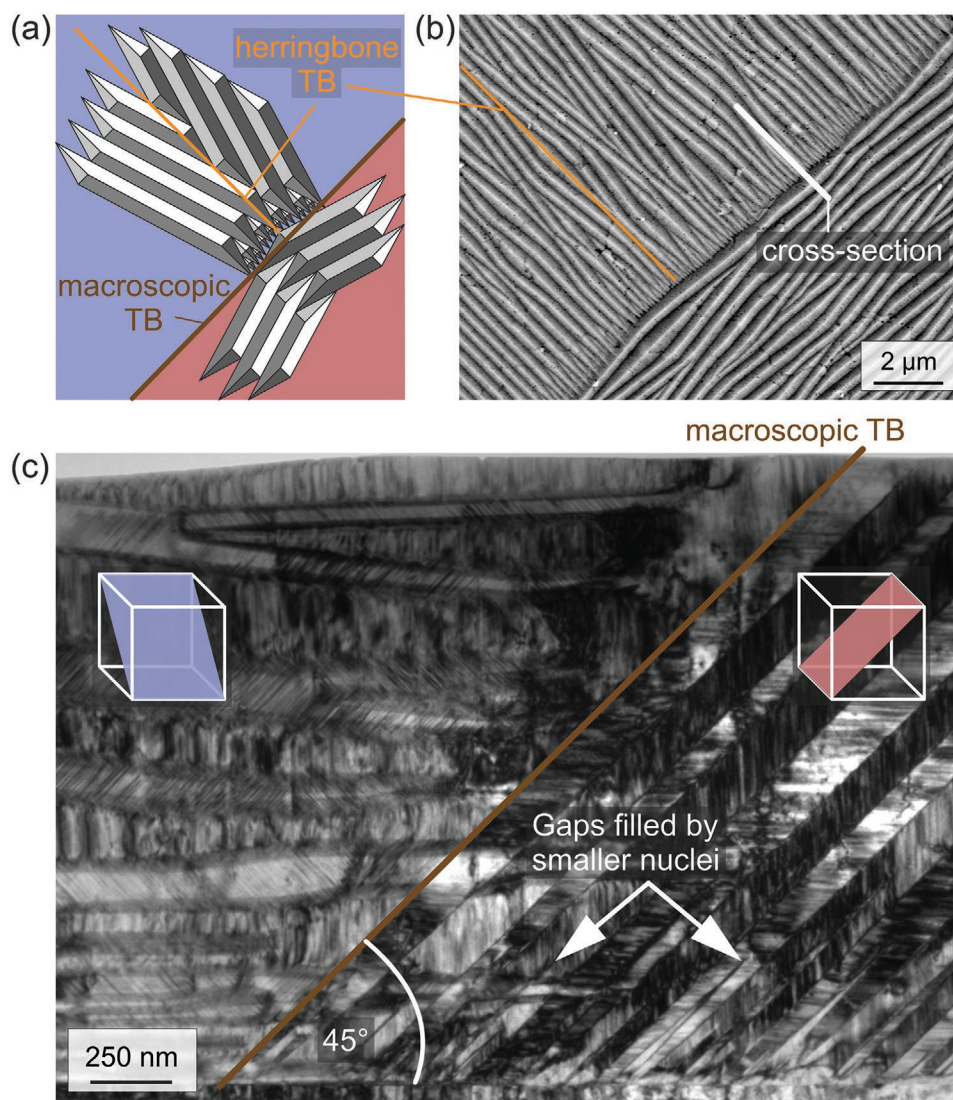FUNCTIONAL
MATERIALS**

www.afm-journal.de

Figure 5. On level 4, coalescence of parallelogram shaped nuclei results in a herringbone laminate, which is the building block for level 5. a) Diamonds and parallelograms on the same $\{1\,1\,0\}_A$ plane are the building blocks for a self-accommodated herringbone laminate (blue background) incorporating herringbone TBs (orange). When nucleation also occurs on a different $\{1\,1\,0\}_A$ plane (red), a macroscopic TB (brown) forms where both herringbone laminates meet. b) SEM micrograph of the type X martensite structure (area marked in Figure 2a). c) TEM cross-section at the position marked in (b). The macroscopic TB separating both herringbone laminates is inclined by 45°. The orientation of the associated austenite $\{1\,1\,0\}_A$ plane is sketched for the left part in blue and for the right part in red (correlating with (a)). The nuclei are inclined according to the sketched planes. In the cross-section, a small angle remains between the nuclei. These gaps are filled up by smaller nuclei refining the martensitic microstructure toward the substrate. This figure without the overlays is given in Figure S6, Supporting Information.

Figure 5c. Due to the cubic symmetry of the austenite, there are six crystallographically equivalent $\{1\,0\,1\}_A$ planes. In principal, the herringbone laminate can occur on any of these six planes, leading to six different orientations. As the martensitic phase transition simultaneously starts in different areas of the sample, differently oriented laminates can form. When two of them meet, their growth will stop, and a macroscopic boundary forms between them. This is depicted in Figure 5a, where the second laminate (red) is rotated by 90° in-plane. These two laminates are connected by the same symmetry operation that also connects the two austenite $\{1\,0\,1\}_A$ planes on which they form. Hence, the connecting boundary is quite similar to a classical TB, and we consider it appropriate to call them macroscopic

TBs. We propose that the spacing between the macroscopic TBs originates from the distribution of microstructural defects that can act as heterogeneous nucleation sites for the martensite.

Macroscopic TBs are incompatible at the atomic scale because the diamonds and parallelograms forming within each herringbone laminate do not fit together with diamonds forming on a different herringbone laminate. Thus, to reduce the gap at the macroscopic TB, faceting can occur, smaller nuclei are introduced (cf. Figure 5a,b), or even some residual austenite may remain well below the transition temperature. Such a disturbed region close to a TB, however, is not unique to macroscopic TBs as it is observed in mesoscopic TBs,[43] too.

To sum up level 5, macroscopic TBs form since the symmetry of austenite allows for all equivalent orientations of herringbone laminates. Their incompatibility implies for a high excess energy, and accordingly they occur only at large spacings.

2.6. Bonus Level: Reciprocal Space

Diffraction experiments are decisive when twinning at the nanoscale occurs, creating a modulated structure.[24a,44] Over the years, many studies were performed with an increasing number of fit parameters used to describe the diffraction pattern.[17c,24a,45] With our scale-bridging approach, one key parameter is sufficient: the tetragonal distortion (c_T/a_T) of the smallest building blocks, which is the well-known parameter describing the transformation along the Bain distortion.[46] In addition to this key parameter, the lattice constant of the austenite a_A (see Figure S3, Supporting Information) is required, assuming volume conservation at the transformation.

We examine the same epitaxial film already used for the real space analysis with its MgO substrate acting as a fixed reference frame. Therefore, we can compare both, arrangement and orientation, of the martensitic variants constructed from the tetragonal building blocks at the nanoscale. Reciprocal space maps (RSM) are used to verify our model of nested building blocks. This method has the advantage that it probes the sample volume, allowing us to obtain statistically relevant data from an X-ray spot of several mm². Therefore, the diffraction image contains a complementary global picture of the local orientation relationships between the martensitic variants in the sample.

To calculate the RSM, we use the c_T/a_T-ratio as key parameter and consider the five levels of building blocks. This is described in the Supporting Information together with further details on the device setup. The comparison between measured and calculated RSM in **Figure 6** reveals a good agreement of diffraction positions and intensity.

This demonstrates that our approach of nested building blocks is suitable to describe the reciprocal space of a hierarchically twinned microstructure. For the calculated RSM, an optimized value for $c_T/a_T = 1.205$ is obtained, as shown in the inset of Figure 6. In Figure S8, Supporting Information, it is demonstrated that the same model also works on a local scale. For this purpose, TEM diffraction images taken for one nucleus of type Y martensite were compared to the variant orientation predicted by the hierarchical model. Thereby, it can be shown that a good agreement between theory and experiment is also observable locally.

3. Preview: Microstructure Design

To optimize the functional properties of materials showing martensitic transitions, designing the microstructure is a crucial point. We therefore look at the levels introduced before and describe how they can be designed. At level 0, the composition can be used to vary the number of valence electrons,[47] which decides on the formation of the different modulated/nonmodulated phases.[48] We can trace this back to a variation of the c_T/a_T-ratio of the tetragonal building blocks as introduced previously.[12] At level 1, this ratio decides which modulated phase forms. Depending on the type of phase, different stress and strain values can be obtained, which allows selecting different properties for actuation by magnetically induced reorientation.[49] In addition, the type of phase is also critical for
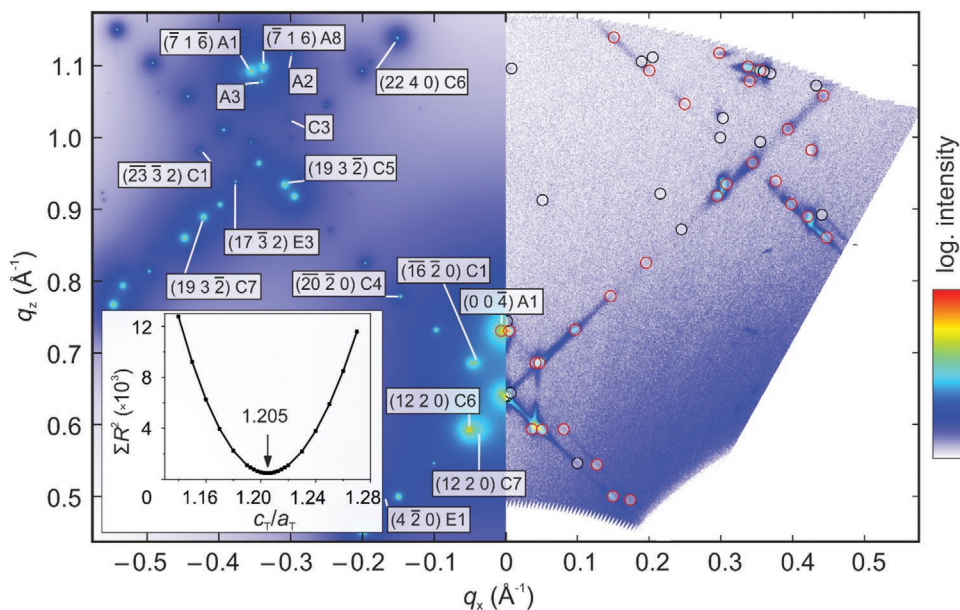

Figure 6. Reciprocal space map (RSM) of a hierarchically twinned microstructure. Measured (right) and calculated (left) RSM along the in-plane (q_x) and out-of-plane (q_z) directions agree well for an optimized c_T/a_T-ratio of 1.205, as summarized in the inset. It depicts the sum of the squared variation R^2 between 30 measured and calculated peak positions when varying the c_T/a_T-ratio. The calculated peak positions are marked in the measured RSM with black and red circles. The red circles indicate the peaks used for the determination of the c_T/a_T-ratio. Only the majority sets A, C, and E are included (see Tables S1 and S2 in the Supporting Information for further details). Indexing of the reflections is described in the Supporting Information as well.

**ADVANCED
SCIENCE NEWS**
www.advancedsciencenews.com

**ADVANCED
FUNCTIONAL
MATERIALS**
www.afm-journal.de

all caloric effects, since a modulation with a narrow spacing of nano-TBs is necessary to minimize hysteresis losses.[50] On level 2, the formation of $(a/b)_{MM}$-TBs is an aspect which is still in the focus of current research.[35] Our investigation proposes that the amount of $(a/b)_{MM}$-twinning can be controlled by the c_T/a_T-ratio, which will allow to examine the impact of these TBs systematically. At level 3 and 4, it is decisive for actuation to obtain type II instead of type I TBs as they exhibit a twinning stress lower by one order of magnitude.[38] Since levels 3 and 4 are governed by nucleation and growth respectively, we propose two measures to control the formation of the herringbone laminate. As a permanent measure, we suggest to utilize the recently identified segregation tendency of Heusler alloys[51] for the formation of defects by precipitations. Depending on size and shape, precipitates can either facilitate nucleation or hinder growth by pinning. As a reversible measure, we propose to adjust cooling rate and temperature gradient for the transition, which allows controlling the kinetics of nucleation and growth on level 3 and 4 separately. Moreover, our concept of nested building blocks as a whole paves the way for a microscopic understanding of the different transformation kinetics observed in martensites, which can be both, athermal and isothermal.[52] This will be decisive for all caloric applications, as the underlying cooling cycle should run at frequencies as high as possible.[53] Furthermore, the size of diamonds and parallelograms on level 4 is limited by incompatible boundaries, which means that they can be controlled for example by grain size, or film thickness in thin films.[42] Thereby, it is for example possible to shift the temperature of the martensitic transition.[54] Lastly, to eliminate macroscopic TBs on level 5, external stress or magnetic fields can be used as they favor particular orientations. This is decisive for magnetically induced reorientation, as incompatible macroscopic TBs hinder any actuation.[55] Overall, our approach of nested building blocks on five levels determines most features of the martensitic microstructure based on the c_T/a_T-ratio from level 0. Nonetheless, we could identify a few paths, which can be utilized to design the remaining features of the hierarchical microstructure.

4. Conclusion: Quest Fulfilled

Our approach of nested building blocks explains the deeply hierarchical microstructure of martensitic materials. We are able to examine and describe this microstructure on all length scales by creating five consecutive levels of hierarchical building blocks. To proceed from one level to the following, a larger building block is created from smaller ones by twinning as summarized in Figure 1. Each level is required to solve a particular constraint of martensitic transformations: the formation of a phase boundary on level 1, fine adjustment of strain at this phase boundary (level 2), nucleation (level 3), growth of martensite (level 4) and level 5 due to the symmetry of the austenite. Adapting each of these constraints requires a local energy minimization at every level instead of a global minimization. Since each level builds upon the previous one, the complete martensitic microstructure can be constructed using the c_T/a_T-ratio of the smallest, tetragonal building block as the key parameter for our model system Ni–Mn–Ga. Furthermore, we could identify the few remaining

possibilities to design such a martensitic microstructure (cf. Section 3: "Preview"). A transfer from our model system toward other Heusler alloys is straightforward as they have the same structure. However, our approach of nested building blocks can be applied to other martensitic materials as well. For this purpose, the different crystal symmetry has to be considered, which defines the initial building block. We expect that our approach is also applicable to other functional materials like ferroelectrics and multiferroics, where similar diffusionless transitions occur. This can help to further design the microstructure of the aforementioned materials considering that a hierarchical microstructure is crucial for the functional properties.

5. Experimental Section

The 2 µm thick epitaxial $Ni_{48}Mn_{33}Ga_{19}$ film was grown by magnetron sputter deposition on single crystalline MgO (0 0 1) as this is an established substrate for this purpose.[22] At first, a 70 nm Cr-buffer layer was deposited underneath the film. The substrate was heated to 300 °C during deposition and slowly cooled to room temperature within the chamber after the deposition. The sample surface was imaged by SEM (FEI Helios NanoLab 600i) using backscattered electron contrast. This dual (ion and electron) beam instrument was also used to prepare two FIB cross-section lamellas for TEM investigations. For the characterizations on the mesoscopic length scale, bright-field TEM was conducted using a FEI Tecnai G2 microscope (ThermoFisher Scientific Comp.) operated at 200 kV acceleration voltage. This device was also used for the TEM diffraction experiments shown in the Supporting Information. For nanoscale (atomic) imaging, aberration-corrected high-resolution TEM was carried out using a double-corrected FEI Titan³ 80–300 microscope (ThermoFisher Scientific Comp.) operated at 300 kV acceleration voltage.

The TEM images in Figures 2b,c, 4d, and 5c were slightly rotated to align the interface between substrate and film parallel to the picture border and then cropped to a rectangle. Brightness and contrast of Figures 2b,c and 4d were slightly optimized, uniformly for the whole image.

Reciprocal space maps (RSM) are a well-established technique to analyze epitaxial thin films as they provide the scattered intensity along a planar cut through the reciprocal space. The cut can be defined by the sample orientation and is almost 2D, just limited by the device apertures. Measurements were performed on a Philips X'Pert X-ray device with a four-circle goniometer using Cu-Kα radiation and an area detector (Malvern Panalytical PIXcel3D). For each measurement, an in-plane rotation angle of the sample ($\varphi = 45°$) and a tilting angle perpendicular to the measurement plane ($\psi = 3.5°$) were specified. The used measurement range was between 0.6° and −28.2° for ω (sample tilt in beam direction) and between 22.5° and 64° for θ (incident angle).

For the MATLAB implementation of the hierarchical model, all five levels established previously were incorporated. All details are described in the Supporting Information including the considerations for the calculation of the RSM cut. In addition, also the MATLAB code is available online.

Supporting Information

Supporting Information is available from the Wiley Online Library or from the author.

Acknowledgements

Conflict of Interest

The authors declare no conflict of interest.

[1] H. Kitahara, R. Ueji, N. Tsuji, Y. Minamino, *Acta Mater.* **2006**, *54*, 1279.
[2] a) K. Otsuka, X. Ren, *Prog. Mater. Sci.* **2005**, *50*, 511; b) M. Nishida, T. Nishiura, H. Kawano, T. Inamura, *Philos. Mag.* **2012**, *92*, 2215.
[3] J. J. Yao, W. W. Ge, L. Luo, J. F. Li, D. Viehland, H. S. Luo, *Appl. Phys. Lett.* **2010**, *96*, 222905.
[4] D. M. Evans, A. Schilling, A. Kumar, D. Sanchez, N. Ortega, M. Arredondo, R. S. Katiyar, J. M. Gregg, J. F. Scott, *Nat. Commun.* **2013**, *4*, 2548.
[5] a) B. Yang, T. Liu, X. Hao, Z. Li, Y. Zhang, G. Qin, M.-J. Philippe, C. Esling, X. Zhao, L. Zuo, *Adv. Eng. Mater.* **2018**, *20*, 1700171; b) R. Niemann, A. Backen, S. Kauffmann-Weiss, C. Behler, U. K. Rößler, H. Seiner, O. Heczko, K. Nielsch, L. Schultz, S. Fähler, *Acta Mater.* **2017**, *132*, 327.
[6] a) V. Srivastava, Y. T. Song, K. Bhatti, R. D. James, *Adv. Energy Mater.* **2011**, *1*, 97; b) M. Gueltig, H. Ossmer, M. Ohtsuka, H. Miki, K. Tsuchiya, T. Takagi, M. Kohl, *Adv. Energy Mater.* **2014**, *4*, 1400751.
[7] J. Liu, T. Gottschall, K. P. Skokov, J. D. Moore, O. Gutfleisch, *Nat. Mater.* **2012**, *11*, 620.
[8] P. O. Castillo-Villa, L. Manosa, A. Planes, D. E. Soto-Parra, J. L. Sanchez-Llamazares, H. Flores-Zuniga, C. Frontera, *J. Appl. Phys.* **2013**, *113*, 053506.
[9] B. Schleicher, R. Niemann, S. Schwabe, R. Hühne, L. Schultz, K. Nielsch, S. Fähler, *Sci. Rep.* **2017**, *7*, 14462.
[10] a) K. Ullakko, J. K. Huang, C. Kantner, R. C. O'Handley, V. V. Kokorin, *Appl. Phys. Lett.* **1996**, *69*, 1966; b) A. Sozinov, N. Lanska, A. Soroka, W. Zou, *Appl. Phys. Lett.* **2013**, *102*, 021902.
[11] R. Kainuma, Y. Imano, W. Ito, Y. Sutou, H. Morito, S. Okamoto, O. Kitakami, K. Oikawa, A. Fujita, T. Kanomata, K. Ishida, *Nature* **2006**, *439*, 957.
[12] A. G. Khachaturyan, S. M. Shapiro, S. Semenovskaya, *Phys. Rev. B* **1991**, *43*, 10832.
[13] A. Zayak, W. A. Adeagbo, P. Entel, V. D. Buchelnikov, *Phase Transitions* **2005**, *78*, 259.
[14] O. Kastner, G. Eggeler, W. Weiss, G. J. Ackland, *J. Mech. Phys. Solids* **2011**, *59*, 1888.
[15] J. M. Ball, R. D. James, *Arch. Ration. Mech. Anal.* **1987**, *100*, 13.
[16] K. Bhattacharya, *Microstructure of Martensite*, Oxford University Press, Oxford **2003**.
[17] a) Z. B. Li, Y. D. Zhang, C. Esling, X. Zhao, L. Zuo, *Acta Mater.* **2012**, *60*, 6982; b) P. Müllner, A. H. King, *Acta Mater.* **2010**, *58*, 5242; c) L. Righi, F. Albertini, E. Villa, A. Paoluzi, G. Calestani, V. Chernenko, S. Besseghini, C. Ritter, F. Passaretti, *Acta Mater.* **2008**, *56*, 4529.
[18] A. L. Roytburd, *Phase Transitions* **1993**, *45*, 1.
[19] M. E. Gruner, R. Niemann, P. Entel, R. Pentcheva, U. K. Rößler, K. Nielsch, S. Fähler, *Sci. Rep.* **2018**, *8*, 8489.
[20] A. Diestel, V. Neu, A. Backen, L. Schultz, S. Fähler, *J. Phys.: Condens. Matter* **2013**, *25*, 266002.
[21] B. Yang, Y. D. Zhang, Z. B. Li, G. W. Qin, X. Zhao, C. Esling, L. Zuo, *Acta Mater.* **2015**, *93*, 205.
[22] M. Thomas, O. Heczko, J. Buschbeck, U. K. Rößler, J. McCord, N. Scheerbaum, L. Schultz, S. Fähler, *New J. Phys.* **2008**, *10*, 023040.
[23] L. Straka, O. Heczko, H. Seiner, N. Lanska, J. Drahokoupil, A. Soroka, S. Fähler, H. Hanninen, A. Sozinov, *Acta Mater.* **2011**, *59*, 7450.
[24] a) J. Pons, V. A. Chernenko, R. Santamarta, E. Cesari, *Acta Mater.* **2000**, *48*, 3027; b) L. Zhou, M. M. Schneider, A. Giri, K. Cho, Y. Sohn, *Acta Mater.* **2017**, *134*, 93.
[25] R. Niemann, S. Fähler, *J. Alloys Compd.* **2017**, *703*, 280.
[26] a) A. Ayuela, J. Enkovaara, K. Ullakko, R. M. Nieminen, *J. Phys.: Condens. Matter* **1999**, *11*, 2017; b) V. V. Godlevsky, K. M. Rabe, *Phys. Rev. B* **2001**, *63*, 134407.
[27] S. Kaufmann, U. K. Rößler, O. Heczko, M. Wuttig, J. Buschbeck, L. Schultz, S. Fähler, *Phys. Rev. Lett.* **2010**, *104*, 145702.
[28] K. Otsuka, C. M. Wayman, *Shape Memory Materials*, Cambridge University Press, Cambridge **1998**.
[29] R. Ranjan, S. Banik, S. R. Barman, U. Kumar, P. K. Mukhopadhyay, D. Pandey, *Phys. Rev. B* **2006**, *74*, 224443.
[30] L. Righi, F. Albertini, G. Calestani, L. Pareti, A. Paoluzi, C. Ritter, P. A. Algarabel, L. Morellon, M. R. Ibarra, *J. Solid State Chem.* **2006**, *179*, 3525.
[31] F. C. Frank, J. H. Van der Merwe, *Proc. R. Soc.* **1949**, *A198*, 205.
[32] P. Bak, *Rep. Prog. Phys.* **1982**, *45*, 587.
[33] A. Zheludev, S. M. Shapiro, P. Wochner, L. E. Tanner, *Phys. Rev. B* **1996**, *54*, 15045.
[34] O. Heczko, L. Klimsa, J. Kopecek, *Scr. Mater.* **2017**, *131*, 76.
[35] L. Straka, J. Drahokoupil, P. Vertat, M. Zeleny, J. Kopecek, A. Sozinov, O. Heczko, *Sci. Rep.* **2018**, *8*, 11943.
[36] L. Straka, J. Drahokoupil, P. Vertat, J. Kopecek, M. Zeleny, H. Seiner, O. Heczko, *Acta Mater.* **2017**, *132*, 335.
[37] Z. B. Li, B. Yang, Y. D. Zhang, C. Esling, X. Zhao, L. Zuo, *IUCrJ* **2019**, *6*, 909.
[38] O. Heczko, L. Straka, H. Seiner, *Acta Mater.* **2013**, *61*, 622.
[39] H. Seiner, private communication.
[40] N. Scheerbaum, Y. W. Lai, T. Leisegang, M. Thomas, J. Liu, K. Khlopkov, J. McCord, S. Fähler, R. Träger, D. C. Meyer, L. Schultz, O. Gutfleisch, *Acta Mater.* **2010**, *58*, 4629.
[41] H. Seiner, P. Plucinsky, V. Dabade, B. Benesova, R. D. James, **2019**, https://arxiv.org/pdf/1910.05235.pdf.
[42] A. Diestel, A. Backen, U. K. Rößler, L. Schultz, S. Fähler, *Appl. Phys. Lett.* **2011**, *99*, 092512.
[43] M. Matsuda, K. Yasumoto, K. Hashimoto, T. Hara, M. Nishida, *Mater. Trans.* **2012**, *53*, 902.
[44] S. Schwabe, B. Schleicher, R. Niemann, R. Hühne, P. Walter, K. Nielsch, A. Waske, S. Fähler, *Energy Technol.* **2018**, *6*, 1453.
[45] S. Singh, V. Petricek, P. Rajput, A. H. Hill, E. Suard, S. R. Barman, D. Pandey, *Phys. Rev. B* **2014**, *90*, 014109.
[46] E. C. Bain, *Trans. Am. Inst. Min. Metall. Eng.* **1924**, *70*, 25.
[47] V. A. Chernenko, *Scr. Mater.* **1999**, *40*, 523.
[48] B. Dutta, A. Cakir, C. Giacobbe, A. Al-Zubi, T. Hickel, M. Acet, J. Neugebauer, *Phys. Rev. Lett.* **2016**, *116*, 025503.
[49] O. Heczko, L. Straka, K. Ullakko, *J. Phys. IV* **2003**, *112*, 959.
[50] R. Niemann, U. K. Rößler, M. E. Gruner, O. Heczko, L. Schultz, S. Fähler, *Adv. Eng. Mater.* **2012**, *14*, 562.
[51] V. V. Sokolovskiy, M. E. Gruner, P. Entel, M. Acet, A. Cakir, D. R. Baigutlin, D. Buchelnikov, *Phys. Rev. Mater.* **2019**, *3*, 084413.
[52] J. W. Christian, *The Theory of Transformations in Metals and Alloys*, Elsevier Science Ltd., Oxford **2002**.
[53] S. Fähler, V. K. Pecharsky, *MRS Bull.* **2018**, *43*, 264.
[54] N. Teichert, A. Auge, E. Yuzuak, I. Dincer, Y. Elerman, B. Krumme, H. Wende, O. Yildirim, K. Potzger, A. Hütten, *Acta Mater.* **2015**, *86*, 279.
[55] L. Straka, O. Heczko, H. Hanninen, *Acta Mater.* **2008**, *56*, 5492.